ROYAL SOCIETY OF CHEMISTRY

EDGE ARTICLE

Check for updates

A TADF sensitizer moiety decorated MR emitter for enhancing spin-flip and anti-ACQ

Xingtian Wang, [ID] [a] Jianxing Chen, [ID] [a] Songqian Ni, [ID] [a] Yu Hu, [ID] [a] Haorun Dai, [ID] [a] Zezhu Xiao, [ID] [a] Weiguo Zhu, [ID] [a] Pi-Tai Chou [ID] *[b] and Xiugang Wu [ID] *[a]

Multiple resonance thermally activated delayed fluorescence (MR-TADF) emitters, mainly constructed from rigid fused polycyclic aromatic hydrocarbon frameworks incorporating boron and nitrogen (B/N), have garnered significant attention attributed to their remarkable optoelectronic properties, such as high efficiency, narrowband emission, and so on. However, the relatively large singlet–triplet energy gap (ΔE_{ST}), small spin–orbit coupling (SOC) matrix elements and planar rigid framework inherent to MR-TADF materials lead to slow reverse intersystem crossing rates (k_{RISC}) and aggregation-caused quenching (ACQ), limiting their practical application in organic light-emitting diodes (OLEDs). This study presents an effective molecular design strategy that integrates a bulky thermally activated delayed fluorescence (TADF) moiety (also as a sensitizer) into a multiple-resonance (MR) framework. This hybrid architecture enables the resulting emitter 4TCzBNCN to exhibit bright green emission with a narrow full width at half maximum (FWHM) of approximately 31 nm, alongside a significantly enhanced k_{RISC} of 4.2×10^{6} s^{-1} and near-unity photoluminescence quantum yield. Therefore, the solution-processable OLEDs achieve a maximum external quantum efficiency (EQE$_{max}$) exceeding 26.8% with an almost unchanged FWHM even at high doping concentration. The results demonstrate that TADF sensitizer decorated MR emitters simultaneously accelerate k_{RISC} and suppress the ACQ effect, thereby addressing a persistent challenge in conventional MR emitters.

1 Introduction

As technological progress ushers society into an intelligent era, display technology has become a crucial interface between smart device functionalities and human interaction. Among various display technologies, OLEDs have gained rapid prominence in recent decades due to their inherent advantages: self-emissive characteristics, fast response speed, true-to-life color reproduction, and mechanical flexibility.[1,2] The organic electroluminescent emitter is a key component in OLEDs, directly influencing display panel performance such as emission color, efficiency, and operational lifetime. The evolution of organic electroluminescent materials has progressed through several generations, including fluorescence, phosphorescence, TADF, and radical emitters.[3] Particularly, TADF emitters possess the advantages of low cost and high efficiency, attracting persistent research enthusiasm. In addition, most TADF-based OLEDs are fabricated using vacuum-deposit methods. In contrast, solution-processed OLEDs provide a compelling alternative, with

benefits including cost-effective production, low equipment requirements, and precise doping concentration.[4–10] Therefore, solution-processed OLEDs incorporating TADF emitters are attracting growing interest in both academic and industrial research, though they tend to exhibit lower external quantum efficiency (EQE) and reduced operational stability compared to vacuum-deposited devices.[11]

Despite achieving near-unity exciton utilization—which enables highly efficient devices—TADF emitters face another challenge: they often suffer from low color purity. The emergence of MR-TADF materials, pioneered by Takuji Hatakeyama *et al.*, effectively addresses the challenge of color purity attributed to their narrowband emission characteristics.[12] The key objective in designing MR-TADF materials lies in employing rational strategies to induce multiple resonance (MR) effects within polycyclic heteroaromatics. The MR effects drive the effective alternative separation of the highest occupied molecular orbital (HOMO) and the lowest unoccupied molecular orbital (LUMO) to induce a small ΔE_{ST}, thereby endowing the resulting material with TADF properties.[13,14] Notably, unlike the long-range charge transfer (LRCT) characteristic of traditional donor–acceptor (D–A) type TADF structures, the HOMO and LUMO in the MR-TADF framework are separated by a distance roughly equivalent to a single chemical bond.[15–20] This gives rise to a typical short-range charge transfer (SRCT) feature within

[a]School of Materials Science and Engineering, Jiangsu Engineering Laboratory of Light-Electricity-Heat Energy-Converting Materials and Applications, Jiangsu Collaborative Innovation Center of Photovoltaic Science and Engineering, Changzhou, 213164, China. E-mail: xgwu16@cczu.edu.cn

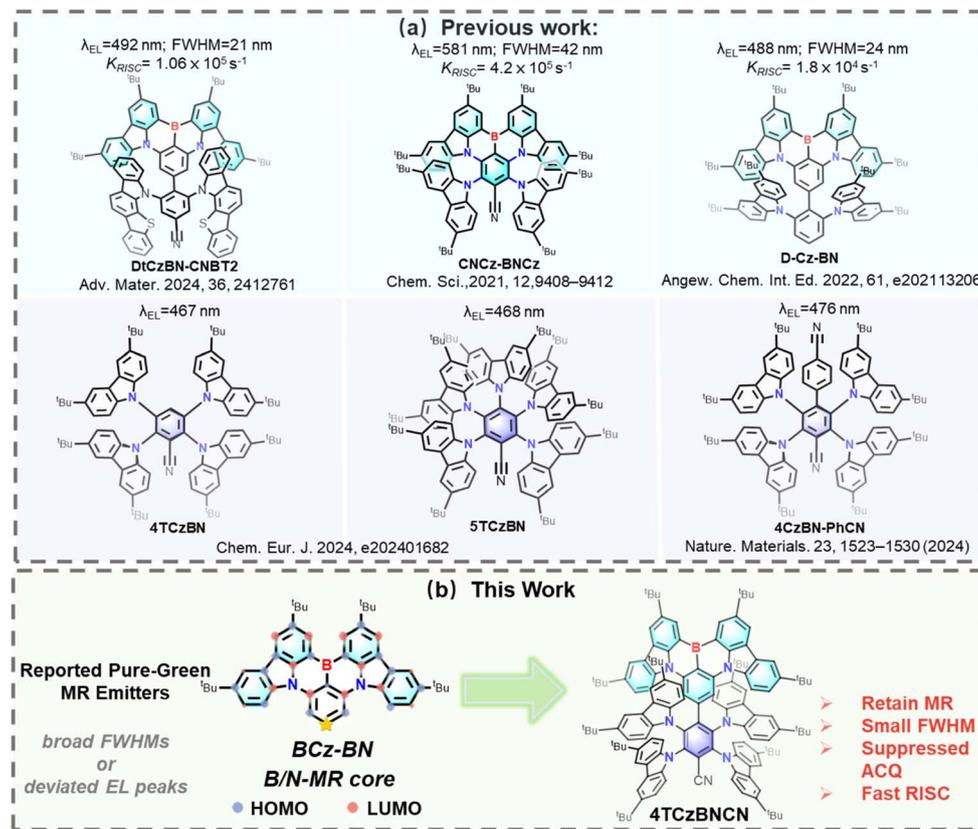*[b]Department of Chemistry, National Taiwan University, Taipei, 10617, Taiwan. E-mail: chop@ntu.edu.tw*

Fig. 1 (a) Previous work. (b) Molecular design strategy of the 4TCzBNCN emitter.

the localized excited state category, which mitigates the potential weakness of radiative transitions caused by the separation of the HOMO and LUMO and is therefore conducive to enhancing the photoluminescence quantum yield (abbreviation: PLQY; symbol: Φ_{PL}). MR-TADF emitters exhibit distinct advantages such as narrow bandwidth emission and high exciton utilization efficiency at low concentrations. However, compared to the D–A type TADF counterparts, the slower reverse intersystem crossing (RISC) process remains a critical bottleneck in many MR emitters due to their SRCT characteristics.[21–30] Another challenge for most MR emitters is their pronounced susceptibility to ACQ arising from their highly planar configurations, which facilitate π–π stacking interactions, thereby leading to doping sensitivity and degrading device performance.[31] To address ACQ, several molecular design strategies have been proposed, including the incorporation of steric substituents to disrupt molecular packing and the use of host–guest doping to spatially separate intermolecular interactions.[32–34] Furthermore, several strategies incorporating auxiliary donor groups or TADF units have been proposed to synergistically address the challenges of ACQ and RISC. For instance, You et al. introduced a functional cyano-unit into the LUMO position of the MR-TADF framework, which can promote attractive red-shifted emission. The resultant CNCZ-BNCZ exhibits an orange-red color due to the strong electron-withdrawing ability of the cyano-group. However, due to its long lifetime of delayed fluorescence (τ_d = 60.4 μs), the triplet

excitons of CNCZ-BNCZ cannot be quickly converted into singlet excitons. This induces significant triplet–triplet annihilation (TTA) at elevated current densities, resulting in a substantial loss of efficiency and pronounced efficiency roll-off.[24] Duan et al. addressed the ACQ issue by encapsulating the MR core with sterically hindered carbazole groups, obtaining the efficient emitter D-Cz-BN. Its corresponding device maintained an external quantum efficiency (EQE) of 36.3% and a narrowband emission spectrum with a FWHM of 24 nm, even at a high doping concentration of 20 wt%. Nevertheless, its k_{RISC} in solution was merely 1.8×10^4 s^{-1}, which is substantially lower than the average values of high-performance TADF materials. Zhang et al. integrated a B/N-MR core with a donor–acceptor (D–A) moiety to construct DtCzBN-CNBT2, which exhibits inherent TADF properties with accelerated k_{RISC} and a suppressed ACQ effect. Nevertheless, these strategies demand meticulous control to strike a delicate balance between preserving a narrow emission bandwidth and retaining TADF characteristics—an inherent trade-off that poses a non-trivial challenge in molecular design.

Herein, we propose a molecular design strategy that integrates a TADF sensitizer moiety, 4TCzBN, into an MR framework. Distinct from previous single-effect design paradigms, our approach constructs a synergistic MR/TADF hybrid architecture. This successfully addresses two persistent challenges in MR-TADF materials, i.e., slow spin-flip dynamics and pronounced ACQ, while offering a straightforward path to

explore sensitizer performance in devices. This approach facilitates a sufficient expansion of the LUMO distribution while maintaining the original HOMO delocalization compared to the parent MR core (BCz-BN).[35] Such a cross-shaped HOMO/LUMO configuration retains a predominant SRCT character and some hybrids of LRCT excited states, thereby accelerating the efficient spin-flip process and red-shifting the emission spectrum toward saturated green light in contrast with BCz-BN. Meanwhile, the encapsulated TADF sensitizer moiety with bulk steric hindrance enhances quenching resistance. As anticipated, the target emitter—denoted as 4TCzBNCN—successfully combines the narrowband emission characteristic of BCz-BN with the prominent TADF behavior of 4TCzBN (Fig. 1). Specifically, 4TCzBNCN exhibits bright green emission with a narrow FWHM of 31 nm.[36] Crucially, green OLEDs based on 4TCzBNCN demonstrate excellent performance across a wide range of doping concentrations. An optimized solution-processed OLED achieves an EQE_{max} exceeding 26.8%, along with an ultra-high luminance of up to 10 320 cd m^{-2}. This work highlights that a TADF sensitizer moiety decorated MR core can synergistically modulate the excited states and provide steric hindrance for the resulting MR-TADF materials, thereby concurrently accelerating the efficient spin-flip process and enhancing ACQ resistance.

2   Results and discussion

4TCzBNCN was synthesized via a two-step reaction sequence from key intermediates DtCzB-Bpin.[37] The key steps for preparing the final material involve the Suzuki coupling reaction between boronic esters and brominated aromatics, as well as the aromatic nucleophilic substitution reaction between fluoroaromatics and 3,6-di-tert-butylcarbazole (tCz), with an overall moderate yield (Fig. S1). The product 4TCzBNCN was sequentially purified by column chromatography and gradient vacuum sublimation. Its chemical structure was confirmed by ^{1}H NMR, ^{13}C NMR spectroscopy, and high-resolution mass

spectrometry (HR-MS). Detailed synthetic procedures and characterization data are provided in the SI.

To further confirm the molecular structure and packing arrangement, single crystals of 4TCzBNCN were cultured using the slow evaporation method from a mixed solvent system of chloroform and methanol. The summarized crystallographic data are presented in Table S1. Single-crystal X-ray analysis shows that the molecular conformation of 4TCzBNCN is highly distorted between its MR core and TADF moiety, leading to an increased intermolecular distance (Fig. 2a). The dihedral angles among the central benzene ring in the MR core and carbazole fragments in benzonitrile range from 52.5° to 74.6°. Notably, no obvious intermolecular π–π stacking interactions are observed among the MR cores in 4TCzBNCN. Instead, the crystal packing is stabilized exclusively through weak van der Waals interactions, such as C–H···C and C–H···H–C short contacts (distances >2.39 Å) involving both the tCz units and the MR core, as well as interactions between vicinal tCz groups, as illustrated in Fig. 2b. The distance of the adjacent MR cores exceeds 10 Å due to the sterically shielded tCz groups on the periphery of the B/N-PAHs (Fig. S7 and S8). This hybrid architecture, combining a planar MR framework with a twisted TADF moiety, synergistically enhances k_{RISC}, suppresses ACQ, and preserves the desirable narrowband emission profile.

The photophysical properties of 4TCzBNCN in toluene solution (1×10^{-5} mol L^{-1}) were analyzed using ultraviolet-visible (UV-Vis) absorption, photoluminescence (PL), and phosphorescence spectra. As shown in Fig. 3a, 4TCzBNCN exhibits intense absorption below 450 nm, attributed mainly to π–π* transitions within its aromatic conjugated segments. The moderate absorption band centered at 483 nm, unlike the characteristic intense transitions observed for BCz-BN (Fig. S15), originates from the cooperative interplay between the SRCT of the MR framework and LRCT associated with the TADF moiety. Its structureless emission peak appears at 506 nm with a minor Stokes shift of 23 nm (0.12 eV) and a FWHM of
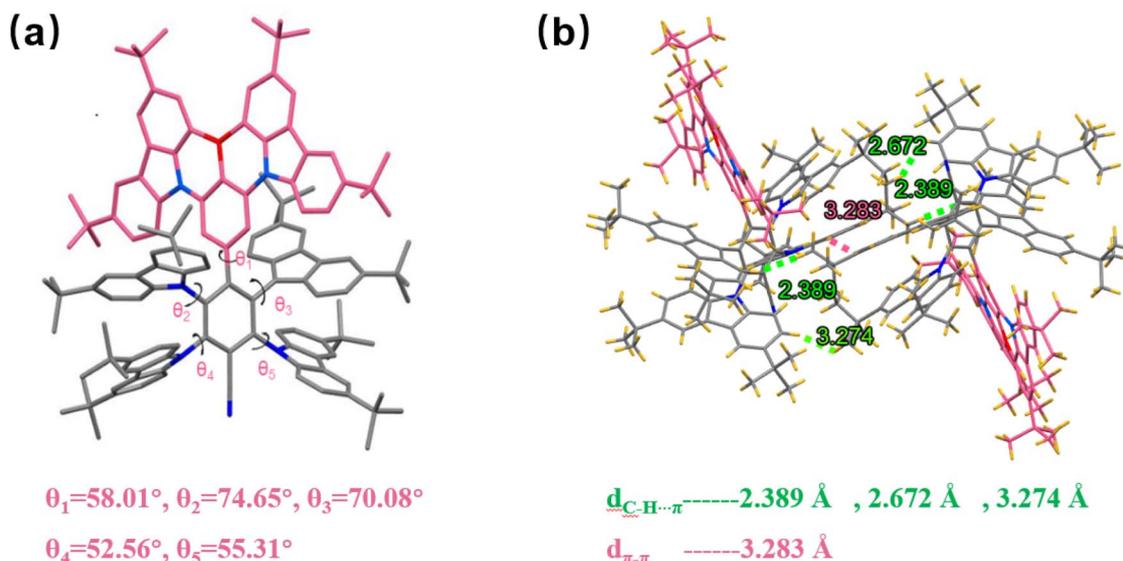

$\theta_1=58.01°$, $\theta_2=74.65°$, $\theta_3=70.08°$
$\theta_4=52.56°$, $\theta_5=55.31°$

$d_{C-H\cdots\pi}$------2.389 Å , 2.672 Å , 3.274 Å
$d_{\pi-\pi}$ ------3.283 Å

Fig. 2   (a) Single-crystal information. (b) Packing diagram of 4TCzBNCN.
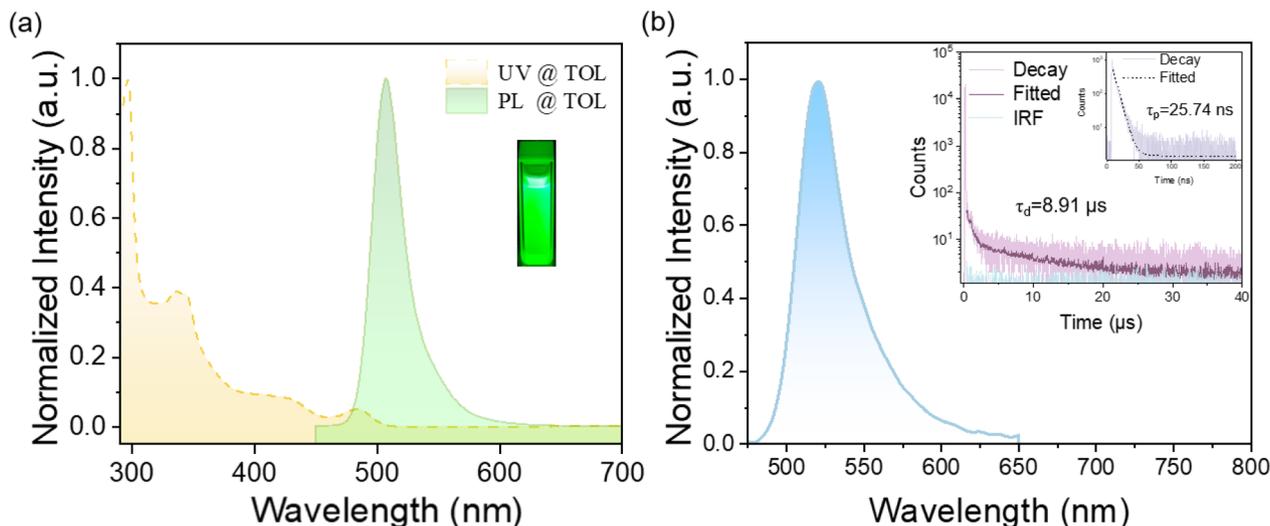
Fig. 3 (a) UV–vis absorption and fluorescence (FL) spectra (300 K) of 4TCzBNCN in toluene solution (1×10^{-5} mol L^{-1}) (inset: photograph taken under 365 nm UV light). (b) Steady state photoluminescence (PL) spectra of 4TCzBNCN (5 wt%) doped in a PhCzBCz film. (Inset) The relaxation dynamics of prompt and delayed fluorescence, monitored at 520 nm.

31 nm, further confirming its hybrid TADF and predominant MR characteristics. With increasing solvent polarity, 4TCzBNCN shows minimal solvatochromism, displaying only slight bathochromic shifts in the emission maximum and a marginal increase in FWHM (Fig. S9). This indicates that 4TCzBNCN maintains the dominant SRCT character, despite the incorporation of the TADF moiety into the MR framework. Furthermore, based on the onset wavelengths of the fluorescence and phosphorescence spectra at low temperature (Fig. S10), the S$_1$ and T$_1$ energy levels of 4TCzBNCN are estimated to be 2.54 eV and 2.51 eV, respectively, corresponding to a very small ΔE_{ST} of 0.03 eV. This tiny energy gap facilitates exciton up-conversion from the T$_1$ state to the S$_1$ state. Remarkably, the PL peak position of 4TCzBNCN remains nearly constant at approximately 509 nm, and its FWHM stays relatively small (37–39 nm) as the doping concentration varies from 1 wt% to 5 wt% (Fig. S11). 4TCzBNCN achieves an impressive photoluminescence quantum yield (PLQY) of 99.4% in doped thin films. The transient photoluminescence (TRPL) decay profile clearly demonstrates its TADF behavior, showing a short prompt fluorescence lifetime (τ_p) of 25.7 ns and a delayed fluorescence lifetime (τ_d) of 8.9 µs, corresponding to a radiative decay rate (k_r) of 3.86×10^7 s^{-1} and a k_{RISC} of 4.2×10^6 s^{-1}, which is over 460 times faster than that of BCz-BN (Fig. 3b, see the detailed calculation method in the Supporting

Information).[38] The associated photophysical data are summarized in Table 1.

Density functional theory (DFT) calculations were performed at the B3LYP/6-31G(d) level to investigate the nature and energies of the frontier molecular orbitals of 4TCzBNCN. For comparison, the parent MR-TADF core BCz-BN was also studied. As shown in Fig. 4a, the HOMO of BCz-BN is predominantly delocalized over the electron-donating nitrogen atom and extends to its adjacent ortho/para-positioned carbons within the PAH framework. In contrast, the LUMO is primarily localized on the electron-accepting boron atom and the complementary carbon sites in its vicinity.[39] After incorporating the TADF segment, the HOMO of 4TCzBNCN remains primarily localized on the MR core BCz-BN. In contrast, the LUMO is not only delocalized across the MR-TADF core, but also extends toward the cyano-group and its directly bonded phenyl ring due to the strong electron-withdrawing nature of the cyano-functionality. This spatial distribution of the LUMO complementarily overlaps with the HOMO, facilitating efficient charge transfer and narrowband emission. Notably, the introduction of tCz groups has minimal impact on the distributions of the FMOs, primarily serving to increase intermolecular spacing. In contrast, the incorporated cyano-acceptor group extends the delocalization of the LUMO. The alternately separated HOMO and LUMO distributions, along with the locally expanded

Table 1 Photophysical properties of 4TCzBNCN

Compound	$\lambda_{abs}{}^a$ [nm]	$\lambda_{em}{}^a$ [nm]	S$_1$/T$_1$/$\Delta E_{ST}{}^b$ [ev]	$\tau_p{}^c$ [ns]	$\tau_d{}^c$ [µs]	$\Phi_{PL}{}^d$ (%)	$k_r{}^e$ [10^7 s^{-1}]	$k_{RISC}{}^f$ [10^4 s^{-1}]	$E_{HOMO}/E_{LUMO}/E_g{}^g$ [eV]
BCz-BN[35]	467	481	2.66/2.53/0.13	8.5	68.8	91	16	0.9	−5.40/−2.85/2.55
4TCzBNCN	485	506	2.54/2.51/0.03	25.74	8.91	99.4	3.86	420	−5.26/−3.07/2.19

^{a} Measured in toluene at a concentration of 1.0×10^{-5} mol L^{-1}. ^{b} S$_1$ and T$_1$ were obtained from the onset of fluorescence and phosphorescence spectra at 77 K, respectively. ^{c} Measured in 5 wt% doped films in PhCzBCz. ^{d} Absolute Φ_{PL} of doped films measured using an integrating sphere. ^{e} k_r denotes the rate constant of fluorescence radiative decay (S$_1$ → S$_0$): $k_r = \Phi_P/\tau_p$. ^{f} k_{RISC} means the rate constant of RISC (T$_1$ → S$_1$), $k_{RISC} = \Phi_d k_F k_{DF}/(k_{ISC}\Phi_F)$. ^{g} Optical bandgap ($E_g$) from the absorption onsets. Data for BCz-BN were taken from ref. 35.
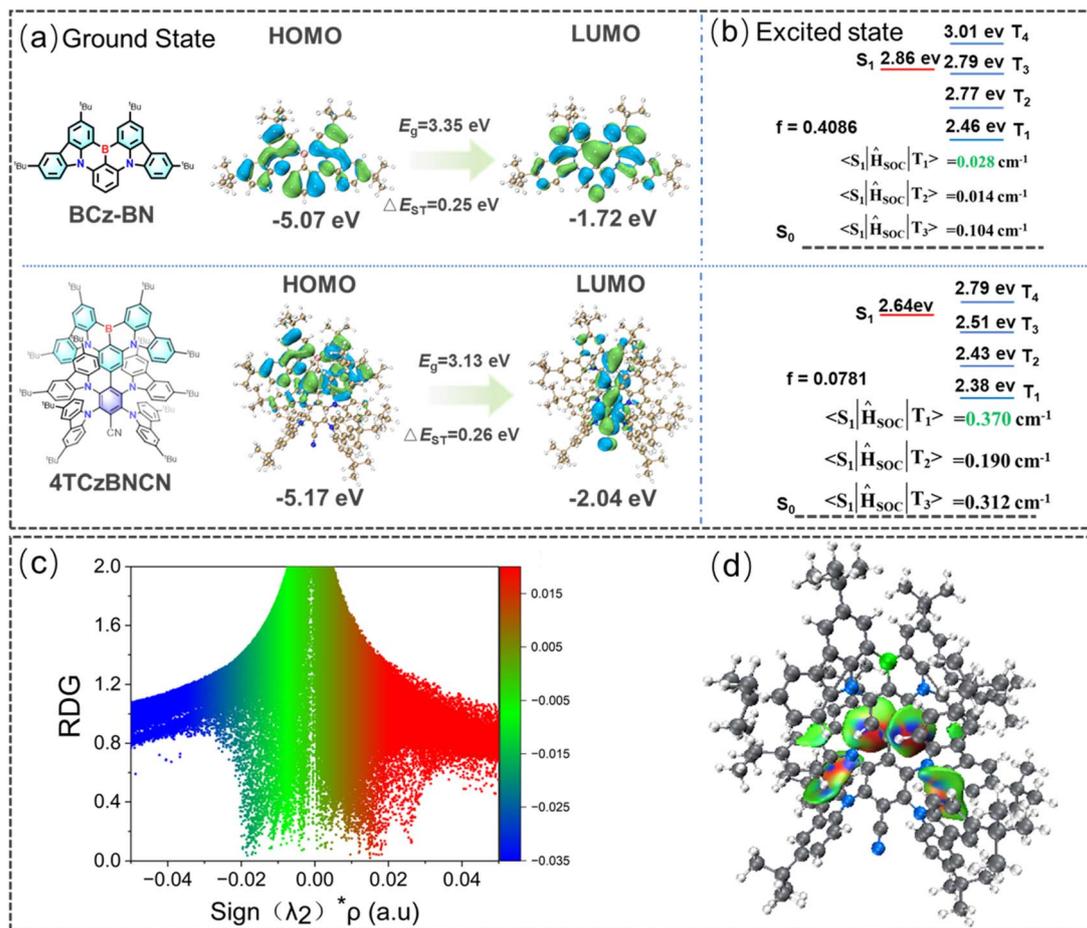
Fig. 4 (a) Frontier molecular orbital distributions (blue for holes and green for electrons), oscillator strengths, and state levels. (b) SOC values in the S_1 geometries of BCz-BN and 4TCzBNCN at the B3LYP/6-31G(d) level. (c) Reduced Density Gradient (RDG) scatter diagrams of 4TCzBNCN. (d) Intramolecular non-covalent interaction (NCI) analysis of 4TCzBNCN.

LUMO orbitals, endow 4TCzBNCN with a predominantly SRCT character and some LRCT contribution. This electronic distribution feature induces a bathochromic shift toward saturated green light and promotes TADF behavior, compared to the parent MR emitter BCz-BN. The calculated HOMO and LUMO energy levels are −5.17 eV and −2.04 eV, respectively, corresponding to an energy gap (E_g) of 3.13 eV (Fig. 4a). Time-dependent density functional theory (TD-DFT) simulations predict a singlet–triplet energy gap (ΔE_{ST}) of 0.26 eV between the S_1 and T_1 states, which is larger than that obtained from experimental data. This result is reasonable; the apparent discrepancy between calculated and experimental ΔE_{ST} values arises from the combined effects of solid-state dielectric stabilization, excited-state conformational relaxation, and multi-state excited-state mixing, which are not fully captured by gas-phase TD-DFT calculations. Based on the computation, Fig. 4 reveals the complete excited-state energy level diagram of 4TCzBNCN and the spin–orbit coupling matrix elements (SOCMEs) between the S_1 and T_n states were evaluated to assess the magnitude of SOC between these states and elucidate the possible RISC channels. Natural transition orbital (NTO) analysis reveals that both the S_1 and T_1 states of 4TCzBNCN possess similar distributions to those of BCz-BN, displaying

predominant SRCT characteristics localized on the B/N core (Fig. 4b and S12 and Table S2). Notably, 4TCzBNCN exhibits strong SOCMEs between its first excited singlet state (S_1) and first excited triplet state (T_1), characterized by a large $|\langle S_1|\hat{H}_{SOC}|T_1\rangle|$ of 0.370 cm^{-1}. This distinguishes it from conventional MR emitters, which typically exhibit larger $|\langle S_1|\hat{H}_{SOC}|T_n\rangle|$ values (where $n \geq 2$); e.g., $|\langle S_1|\hat{H}_{SOC}|T_3\rangle|$ is the strongest for BCz-BN. However, the T_2 (2.43 eV), T_3 (2.51 eV), and T_4 (2.79 eV) states clearly exhibit LRCT character, delocalizing from the B/N core to the peripheral tCz units (Fig. S12). These triplet states lie in proximity to the S_1 state (2.64 eV) with smaller energy gaps of 0.13–0.19 eV. Consequently, this system not only efficiently drives the $T_1 \rightarrow S_1$ spin-flip process but also may open new avenues to the spin-flip process via T_n ($n \geq 2$) → S_1 due to the spaced upper triplet states (T_2–T_4) close to S_1 and the moderate SOCMEs between them, suggesting potential RISC channels that could enhance the overall TADF performance and accelerate the k_{RISC}. Reduced density gradient (RDG) function calculations indicate that the introduction of tCz groups leads to a locally highly twisted molecular conformation, enhancing intramolecular non-covalent interactions (NCIs, i.e., short interactions, see Fig. 4c).[40–42] To visualize the spatial distribution of NCIs within the molecule, color-mapped RDG
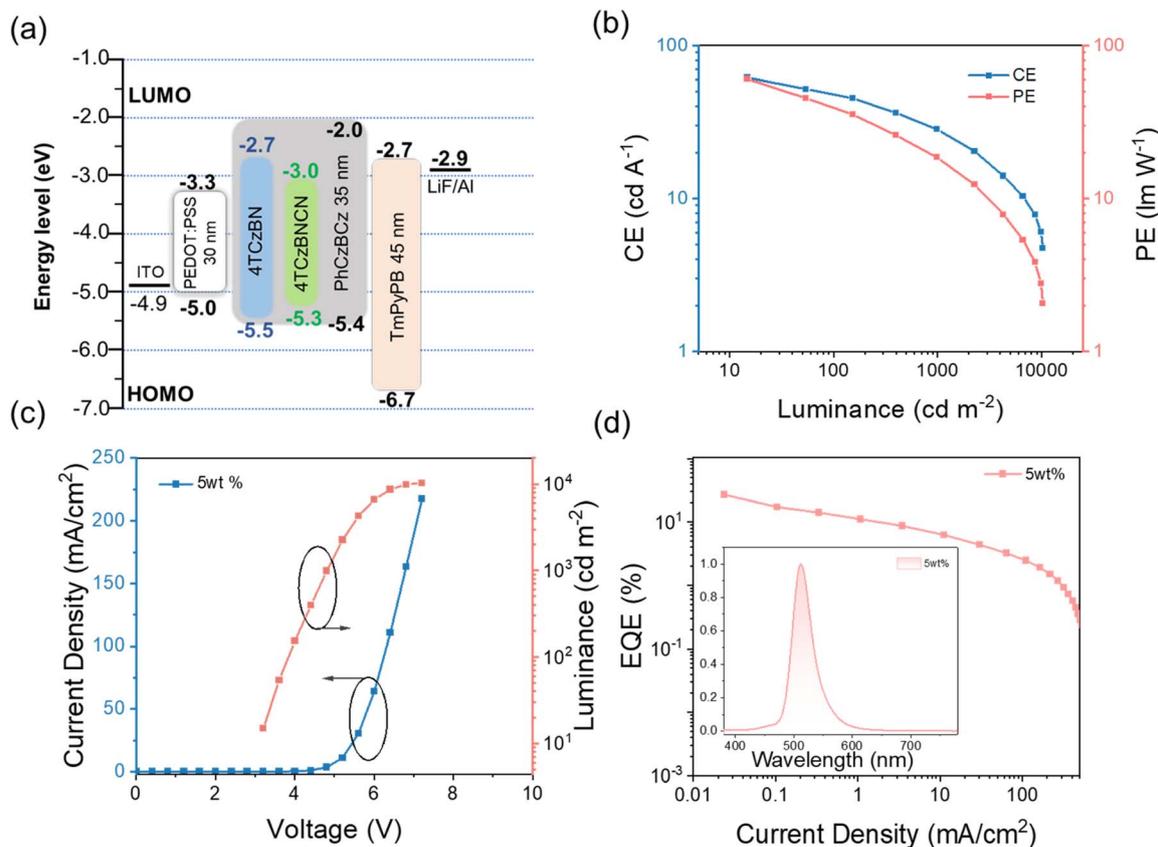
Fig. 5 Solution-processed HF-OLED performance based on 5 wt% 4TCzBNCN doped emitting layers: (a) device architectures and energy level of the functional layer. (b) PE–luminance–CE curves. (c) Current density and luminance *versus* voltage (*J–V–L*) characteristics. (d) External quantum efficiency (EQE)–luminance curves and EL spectra.

iso-surface plots were generated (Fig. 4d). These plots clearly show that intramolecular NCIs are primarily distributed between the TADF segments and the BCz-BN core, thereby interrupting intermolecular interactions among adjacent B/N cores. This twisted molecular conformation not only provides additional transition channels with LRCT character but also suppresses the ACQ.[43] Moreover, the synergistic effect of the enhanced LRCT component mixed with the inherent SRCT character of the MR core likely contributes to reducing ΔE_{ST} and increasing SOC strength, ultimately promoting an efficient RISC process.[44]

To achieve its potential OLEDs applications, the electrochemical properties and thermal stability of 4TCzBNCN were systematically tested before device fabrication. Based on cyclic voltammetry measurements (Fig. S13), the HOMO and LUMO energy levels of 4TCzBNCN are determined to be −5.45 eV and −3.27 eV, respectively. Moreover, 4TCzBNCN exhibits excellent thermal stability, showing a 5% weight loss temperature (T_d) as high as 478 °C according to thermogravimetric analysis (TGA) (Fig. S14).

To evaluate the electroluminescence (EL) performance of 4TCzBNCN, devices were fabricated with the following configuration according to the matched energy level: ITO/PEDOT: PSS (35 nm)/EML (30 nm)/TmPyPB (50 nm)/LiF (1 nm)/Al (120 nm). PEDOT: PSS and LiF serve as the hole injection layer (HIL) and

the electron injection layer (EIL), respectively. TmPyPB acts as an electron transport layer (ETL). The corresponding chemical structures of the materials used in the devices and the energy level diagram are shown in Fig. S16 and 5a, respectively. A ternary emitting layer (EML) was constructed, comprising the sensitizer 4TCzBN and host material PhCzBCz. The terminal emitter 4TCzBNCN was doped at concentrations ranging from 1 wt% to 15 wt% to systematically evaluate the corresponding device performance. Notably, the TADF sensitizer 4TCzBN within the 4TCzBNCN architecture exhibits emission spectral overlap with the absorption profile of the terminal emitter (Fig. S16). Based on the Förster resonance energy transfer (FRET) model, the energy transfer from 4TCzBN to 4TCzBNCN was quantitatively analyzed according to eqn (S4)–(S8).[45] A high energy-transfer efficiency (Φ_{ET}) of 94.59% and a fast transfer rate (k_{ET}) of 7.19×10^9 s^{-1} explain the nearly complete quenching of donor emission in the co-doped films.[46,47] As the doping concentration increased, the EL spectra of the 4TCzBNCN-based devices show a slight red shift from 508 nm to 516 nm even in the non-doped state, while the FWHM remains at around 40 nm (Fig. S17 and Table S3). The non-monotonic evolution of FWHM with doping concentration reflects a competition between spectral purity *via* efficient energy transfer and inhomogeneous broadening induced by increased intermolecular interactions at higher concentrations.

Table 2 Summary of electroluminescence data for optimized OLEDs

Devices	V_{on}^a [V]	L_{max}^b [cd m^{-2}]	CE_{max}^c [cd A^{-1}]	PE_{max}^c [lm W^{-1}]	EQE^d [%]	Peak^e [nm]	FWHM^e [nm]	CIE^e [x, y]
5 wt%	3.2	10 320	61.7	60.4	26.8	512	38	(0.16, 0.63)

[a] Turn-on voltage. [b] Maximum luminance. [c] Maximum current efficiency and power efficiency. [d] Maximum EQE. [e] EL peak, FWHM, and CIE color coordinates.

4TCzBNCN-based solution-processed devices achieve optimal EL performance at a 5 wt% doping concentration. The optimum arises from a trade-off between efficient exciton harvesting and the suppression of concentration-induced non-radiative losses, enabled by the sterically protected TADF-sensitizer-decorated MR architecture. Based on the current density and luminance *versus* voltage (*J–V–L*) characteristics, the turn-on voltage is observed to be 3.2 V. Meanwhile, the device achieves an EQE$_{max}$ of 26.8%, a maximum current efficiency (CE) of 61.7 cd A^{-1}, a maximum power efficiency (PE) of 60.4 lm W^{-1}, and a maximum luminance of 10 320 cd m^{-2} (Fig. 5b–d and Table 2). The electroluminescence is similar to that of photoluminescence, peaking at 512 nm with a small FWHM value of 38 nm and CIE coordinates of (0.16, 0.63) (Fig. S17 and Table S3). These high values originate from a high PLQY of 99.4% and a fast k_{RISC}. Despite the modest LT50 measured at 1000 cd m^{-2} under non-ideal conditions (Fig. S18), the overall device performance ranks among the best reported for solution-processed OLEDs, thereby validating the proposed strategy of decorating MR emitters with a TADF sensitizer moiety.

3 Conclusions

In this work, we propose a simple yet effective strategy for designing highly efficient green TADF molecules based on a TADF sensitizer moiety decorated MR core. Both experimental and computational findings confirm that this molecular design strategy not only successfully facilitates k_{RISC} and suppresses ACQ, but also preserves the characteristic narrowband emission and high performance intrinsic to MR emitters. As a result, the target molecule, 4TCzBNCN, exhibits high-quality green emission centered at 506 nm with a narrow FWHM of 30 nm, alongside a significantly accelerated k_{RISC} over 460 times faster than that of the parent MR emitter BCz-BN. Furthermore, by adopting a self-sensitizer moiety, 4TCzBN, as the sensitizer, the resulting device achieves an EQE$_{max}$ of 26.8% and a L_{max} of 10 320 cd m^{-2}, which is outstanding in solution-processed OLEDs. Such a synergistic strategy, combining hybrid MR emitter characteristics to preserve a narrow emission bandwidth with a TADF sensitizer segment to accelerate k_{RISC} and suppress the ACQ effect, lays a solid foundation for fabrication of superior color purity and easy-processability devices.

Author contributions

Xingtian Wang mainly conducted the experiments, analysed the data, and wrote the manuscript. The manuscript was written through the contributions of all authors. All authors have approved the final version of the manuscript. Xiugang Wu and Pi-Tai Chou provided conceptualization and wrote the original draft, as well as reviewed and edited the manuscript.

Conflicts of interest

The authors declare no conflicts of interest.

Data availability

CCDC 2481073 contains the supplementary crystallographic data for this paper.[48]

The data supporting this article have been included within the article or as part of the supplementary information (SI). Supplementary information: experimental methods, synthetic procedures, NMR and mass spectrometry data of the compounds, crystallographic data, theoretical calculation data, photophysical data and device performance data. See DOI: https://doi.org/10.1039/d5sc08829a.

Acknowledgements

Notes and references

1 C. W. Tang and S. A. VanSlyke, *Appl. Phys. Lett.*, 1987, **51**, 913–915.

2 Y. Huang, E.-L. Hsiang, M.-Y. Deng and S.-T. Wu, *Light Sci. Appl.*, 2020, **9**, 105.

3 G. Hong, X. Gan, C. Leonhardt, Z. Zhang, J. Seibert, J. M. Busch and S. Bräse, *Adv. Mater.*, 2021, **33**, 2005630.

4 D. H. Ahn, S. W. Kim, H. Lee, I. J. Ko, D. Karthik, J. Y. Lee and J. H. Kwon, *Nat. Photonics*, 2019, **13**, 540–546.

5 N. Ikeda, S. Oda, R. Matsumoto, M. Yoshioka, D. Fukushima, K. Yoshiura, N. Yasuda and T. Hatakeyama, *Adv. Mater.*, 2020, **32**, 2004072.

6 K. Kishore Kesavan, J. Jayakumar, M. Lee, C. Hexin, S. Sudheendran Swayamprabha, D. Kumar Dubey, F.-C. Tung, C.-W. Wang and J.-H. Jou, *Chem. Eng. J.*, 2022, **435**, 134879.

7 B. Li, Z. Yang, W. Gong, X. Chen, D. W. Bruce, S. Wang, H. Ma, Y. Liu, W. Zhu, Z. Chi and Y. Wang, *Adv. Opt. Mater.*, 2021, **9**, 2100180.

8 Y. Liu, L. Hua, Z. Zhao, S. Ying, Z. Ren and S. Yan, *Adv. Sci.*, 2021, **8**, 2101326.

9 W. Zeng, T. Zhou, W. Ning, C. Zhong, J. He, S. Gong, G. Xie and C. Yang, *Adv. Mater.*, 2019, **31**, 1901404.

10 J. Zhang, Y. Wei and H. Xu, *Nano Energy*, 2021, **83**, 105746.

11 S. Ji, G. Xie and Q. Xue, *Flexible Printed Electron.*, 2023, **8**, 033003.

12 T. Hatakeyama, K. Shiren, K. Nakajima, S. Nomura, S. Nakatsuka, K. Kinoshita, J. Ni, Y. Ono and T. Ikuta, *Adv. Mater.*, 2016, **28**, 2777–2781.

13 Y. Zhang, D. Zhang, J. Wei, Z. Liu, Y. Lu and L. Duan, *Angew. Chem., Int. Ed.*, 2019, **58**, 16912–16917.

14 D. Zhang, M. Cai, Y. Zhang, D. Zhang and L. Duan, *Mater. Horiz.*, 2016, **3**, 145–151.

15 Y. Kondo, K. Yoshiura, S. Kitera, H. Nishi, S. Oda, H. Gotoh, Y. Sasada, M. Yanai and T. Hatakeyama, *Nat. Photonics*, 2019, **13**, 678–682.

16 M. Suresh, E. Duda, D. Hall, Z. Yao, S. Bagnich, A. M. Z. Slawin, H. Bassler, D. Beljonne, M. Buck and Y. Olivier, *J. Am. Chem. Soc.*, 2020, **142**, 6588–6599.

17 J. A. Knöller, G. Meng, X. Wang, D. Hall, A. Pershin, D. Beljonne, Y. Olivier, S. Laschat, E. Zysman-Colman and S. Wang, *Angew. Chem., Int. Ed.*, 2020, **59**, 3156–3160.

18 J. Park, K. J. Kim, J. Lim, T. Kim and J. Y. Lee, *Adv. Mater.*, 2022, **34**, 2108581.

19 J. Bian, S. Chen, L. Qiu, R. Tian, Y. Man, Y. Wang, S. Chen, J. Zhang, C. Duan, C. Han and H. Xu, *Adv. Mater.*, 2022, **34**, 2110547.

20 P. Keerthika and R. K. Konidena, *Adv. Opt. Mater.*, 2023, **11**, 2301732.

21 X. Liang, Z.-P. Yan, H.-B. Han, Z.-G. Wu, Y.-X. Zheng, H. Meng, J.-L. Zuo and W. Huang, *Angew. Chem., Int. Ed.*, 2018, **57**, 11316–11320.

22 M. Yang, I. S. Park and T. Yasuda, Full-Color, *J. Am. Chem. Soc.*, 2020, **142**, 19468–19472.

23 Y. Zhang, J. Wei, D. Zhang, C. Yin, G. Li, Z. Liu, X. Jia, J. Qiao and L. Duan, *Angew. Chem., Int. Ed.*, 2022, **61**, e202113206.

24 Y. Liu, X. Xiao, Y. Ran, Z. Bin and J. You, *Chem. Sci.*, 2021, **12**, 9408–9412.

25 X. Cai, J. Xue, C. Li, B. Liang, A. Ying, Y. Tan, S. Gong and Y. Wang, *Angew. Chem., Int. Ed.*, 2022, **61**, e202200337.

26 Y.-C. Cheng, X.-C. Fan, F. Huang, X. Xiong, J. Yu, K. Wang, C.-S. Lee and X.-H. Zhang, *Angew. Chem., Int. Ed.*, 2022, **61**, e202212575.

27 Y. Zou, J. Hu, M. Yu, J. Miao, Z. Xie, Y. Qiu, X. Cao and C. Yang, *Adv. Mater.*, 2022, **34**, 2201442.

28 D. Chen, H. Wang, D. Sun, S. Wu, K. Wang, X.-H. Zhang and E. Zysman-Colman, *Adv. Mater.*, 2024, **36**, 2412761.

29 Z. Xiao, Y. Zou, Z. Chen, J. Miao, Y. Qiu, Z. Huang, X. Cao, X. Peng and C. Yang, *Adv. Mater.*, 2025, **37**, 2419601.

30 X. Wu, B.-K. Su, D.-G. Chen, D. Liu, C.-C. Wu, Z.-X. Huang, T.-C. Lin, C.-H. Wu, M. Zhu, E. Y. Li, W.-Y. Hung, W. Zhu and P.-T. Chou, *Nat. Photonics*, 2021, **15**, 780–786.

31 X. Wu, S. Ni, C.-H. Wang, W. Zhu and P.-T. Chou, *Chem. Rev.*, 2025, **125**, 6685–6752.

32 F.-M. Xie, H.-Z. Li, K. Zhang, H.-Y. Wang, Y.-Q. Li and J.-X. Tang, *ACS Appl. Mater. Interfaces*, 2023, **15**, 39669–39676.

33 R.-Z. An, F.-M. Zhao, C. Shang, M. Zhou and L.-S. Cui, *Angew. Chem., Int. Ed.*, 2025, **64**, e202420489.

34 R.-Z. An, Y. Sun, H.-Y. Chen, Y. Liu, A. Privitera, W. K. Myers, T. K. Ronson, A. J. Gillett, N. C. Greenham and L.-S. Cui, *Adv. Mater.*, 2024, **36**, 2313602.

35 Y. Xu, Z. Cheng, Z. Li, B. Liang, J. Wang, J. Wei, Z. Zhang and Y. Wang, *Adv. Opt. Mater.*, 2020, **8**, 1902142.

36 C. Li, K. Zhang, Y. Luo, Y. Yang, Y. Huang, M. Jia, Y. He, Y. Lei, J.-X. Tang, Y. Huang and Z. Lu, *Chem. Sci.*, 2024, **15**, 4790–4796.

37 Y. Xu, C. Li, Z. Li, J. Wang, J. Xue, Q. Wang, X. Cai and Y. Wang, *CCS Chem.*, 2021, **4**, 2065–2079.

38 K. Masui, H. Nakanotani and C. Adachi, *Org. Electron.*, 2013, **14**, 2721–2726.

39 Z. Huang, H. Xie, J. Miao, Y. Wei, Y. Zou, T. Hua, X. Cao and C. Yang, *J. Am. Chem. Soc.*, 2023, **145**, 12550–12560.

40 T. Lu and Q. Chen, *Chem.: Methods*, 2021, **1**, 231–239.

41 X.-K. Chen, B. W. Bakr, M. Auffray, Y. Tsuchiya, C. D. Sherrill, C. Adachi and J.-L. Bredas, *J. Phys. Chem. Lett.*, 2019, **10**, 3260–3268.

42 C.-C. Peng, S.-Y. Yang, H.-C. Li, G.-H. Xie, L.-S. Cui, S.-N. Zou, C. Poriel, Z.-Q. Jiang and L.-S. Liao, *Adv. Mater.*, 2020, **32**, 2003885.

43 X.-L. Chen, J.-H. Jia, R. Yu, J.-Z. Liao, M.-X. Yang and C.-Z. Lu, *Angew. Chem., Int. Ed.*, 2017, **56**, 15006–15009.

44 Z. Pei, Q. Ou, Y. Mao, J. Yang, A. d. l. Lande, F. Plasser, W. Liang, Z. Shuai and Y. Shao, *J. Phys. Chem. Lett.*, 2021, **12**, 2712–2720.

45 J. Lim, K. Y. Hwang, S. Y. Kwak, S. M. Cho, J. M. Kim and J. Y. Lee, *Adv. Opt. Mater.*, 2023, **11**, 2300672.

46 Y.-Z. Li, H.-C. Liang, C.-H. Chen, C.-H. Chiu, L.-C. Huang, Y.-T. Lee, Y.-C. Dzeng, C. Chen, B.-Y. Lin, J.-H. Lee, T.-L. Chiu and M.-k. Leung, *Chem. Eng. J.*, 2024, **498**, 155553.

47 X. Song, X. Li, X. Ye, Y. Xie, Y. Zhang, L. Duan and Z. Li, *Adv. Opt. Mater.*, 2025, **13**, 2500515.

48 CCDC 2481073: Experimental Crystal Structure Determination, 2026, DOI: 10.5517/ccdc.csd.cc2p8rmc.